

# Hubbard Model on the Pyrochlore Lattice: a 3D Quantum Spin Liquid

B. Normand<sup>1</sup> and Z. Nussinov<sup>2</sup>

<sup>1</sup>*Department of Physics, Renmin University of China, Beijing 100872, China*

<sup>2</sup>*Department of Physics, Washington University, St. Louis, MO 63160, U.S.A.*

(Dated: September 4, 2018)

We demonstrate that the insulating one-band Hubbard model on the pyrochlore lattice contains, for realistic parameters, an extended quantum spin-liquid phase. This is a three-dimensional spin liquid formed from a highly degenerate manifold of dimer-based states, which is a subset of the classical dimer coverings obeying the ice rules. It possesses spinon excitations, which are both massive and deconfined, and on doping it exhibits spin-charge separation. We discuss the realization of this state in effective  $S = 1/2$  pyrochlore materials.

PACS numbers: 75.10.Jm, 75.10.Kt, 75.40.-s, 75.40.Gb

The quantum spin liquid [1] has become the focal point for our understanding of many of the most fundamental issues in strongly correlated systems. These include exotic quantum phases, quantum critical physics, the relevance of broken symmetries, topological order, entanglement, and the possibly fractional nature of elementary excitations in both gapped and gapless states [2]. The search for theoretical realizations of these ideas has led to numerous proposed models, which while highly informative have generally been too simple or abstract to apply to real materials [3]. The search for materials realizations is a very active field where much current attention is focused on kagome systems [4], triangular organics [5], and other frustrated  $S = 1/2$  and  $S = 1$  quantum magnets. However, materials complexities such as impurities, Dzyaloshinskii-Moriya interactions, spin-orbit coupling, and other anisotropies in real and spin space have to date caused strong departures from theoretical ideals.

Frustrated quantum magnets offer one of the most promising routes to spin-liquid behavior [1, 2]. Frustration presents a formidable barricade to theoretical understanding, because the ground manifold is quite generally a set of highly degenerate basis states, with little or no separation emerging in an exact treatment of the interactions [6]. Numerical calculations converge very slowly due to this proliferation of near-ground states [7]. Fluctuations in such a manifold may lead to a range of exotic phenomena [8–10], and the departures mentioned above are strong because any perturbation is strongly relevant in a highly degenerate system. Few exact results are available, although these afford essential insight [11–14].

In this Letter, we discuss the one-band Hubbard model, showing that on a half-filled pyrochlore lattice it gives a highly frustrated intratetrahedral spin model with only weak perturbations. This model contains an exactly solvable Klein point, about which there is an extended region of parameter space where the ground state is a three-dimensional (3D) quantum spin liquid. This state hosts massive spinon excitations, which are deconfined and move in all three dimensions within the lattice. The parameter range for the spin-liquid phase lies exactly

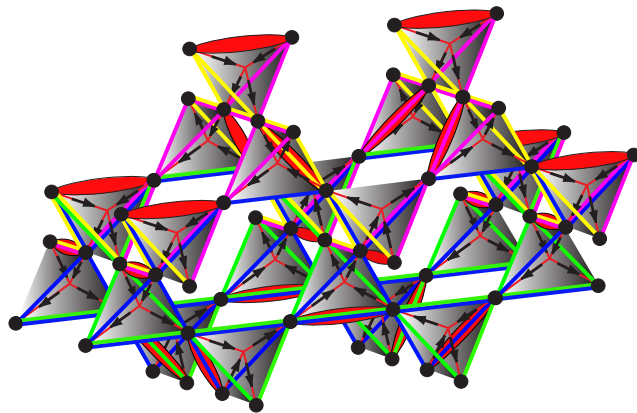


FIG. 1: (color online) Pyrochlore lattice. The magnetic ions (black circles) form a 3D array of corner-sharing tetrahedra.

in the regime of many magnetic materials.

The pyrochlore lattice, shown in Fig. 1, is a 3D array of corner-sharing tetrahedra, has cubic symmetry, and is a geometry widespread in transition-metal and rare-earth oxides. Most such materials have half-filled bands and are Mott-Hubbard insulators due to their interactions. We begin with the Hubbard model,

$$H_{\text{Hubb}} = -t \sum_{\langle ij \rangle, \sigma} c_{i\sigma}^\dagger c_{j\sigma} + U \sum_i n_{i\uparrow} n_{i\downarrow}, \quad (1)$$

where  $c_{i\sigma}^\dagger$  creates an electron at site  $i$  with spin  $\sigma$  and  $n_{i\sigma} = c_{i\sigma}^\dagger c_{i\sigma}$  is the number operator. We use it to discuss the spin liquid with no theoretical abstractions and with controlled approximations. A perturbative expansion in  $t/U$  for the half-filled band leads to

$$H = H_t + J_3 \sum_{\langle\langle ij \rangle\rangle} \vec{S}_i \cdot \vec{S}_j + \mathcal{O}(t^6/U^5), \quad (2)$$

where  $\langle\langle ij \rangle\rangle$  denotes next-neighbor site pairs and

$$H_t = \sum_l [\frac{1}{2} J_1 \mathbf{S}_{l,\text{tot}}^2 + \frac{1}{4} J_2 \mathbf{S}_{l,\text{tot}}^4] \quad (3)$$

is a sum of purely intratetrahedral spin interactions written in terms of the total spin  $\mathbf{S}_{l,\text{tot}} = \mathbf{S}_{l1} + \mathbf{S}_{l2} + \mathbf{S}_{l3} + \mathbf{S}_{l4}$

on each tetrahedron,  $l$  [15]. In Eqs. (2) and (3),

$$J_1 = 4t^2/U - 160t^4/U^3 + \mathcal{O}(t^6/U^5), \quad (4)$$

$$J_2 = 40t^4/U^3 + \mathcal{O}(t^6/U^5), \quad J_3 = 4t^4/U^3 + \mathcal{O}(t^6/U^5),$$

the very large prefactors in  $J_1$  and  $J_2$  arising from the many permutations of fourth-order processes within the tetrahedron. Thus  $J_3 \ll J_{1,2}$  and to an excellent approximation one has an intratetrahedral Hamiltonian  $H_t$ , with only weak interactions coupling spins in different tetrahedra.

$H_t$  (3) has a unique point for one particular parameter ratio,  $J_2 = J_{2c} = -J_1$ , occurring when  $t/U = 1/\sqrt{30}$ , where all singlet and triplet states of the four spins on each tetrahedron have energy zero [17]. Thus any tetrahedron containing a dimer, a singlet ( $S = 0$ ) state of any two spins, and represented by red ellipses in Figs. 1 and 2, has energy zero. Further, because the number of dimers equals the number of tetrahedra on the pyrochlore, all states of the whole system with precisely one dimer per tetrahedron (Fig. 1) are exact, zero-energy ground states. The set of classical dimer coverings maps exactly to the six-vertex model, represented by the six possible “two-in, two-out” configurations of the black arrows in Figs. 2(a) and (b), and hence to the ice problem. Pauling deduced an exponential lower bound on the number of states in this ground manifold,  $N_g > (3/2)^{N/2}$  with  $N$  the system volume (number of tetrahedra) [16], proving that it has extensive degeneracy. This is a Klein point [12, 17]. It is a dimer liquid with algebraic correlations, a classical critical point at which all (of the exponentially many) states are connected by local dimer fluctuations. The excitations created by breaking a dimer are two massive spinons, which propagate freely [15].

However, it is unrealistic to expect any physical system to be exactly at the Klein point. To understand which of its many properties may be preserved in a real material, it is essential to analyze the effect of perturbations. Because every site must be part of one dimer, the quantum mechanical fluctuations of the dimer liquid are local rearrangement processes on a closed path. Figure 2(d) illustrates the minimal possible dimer rearrangement on the pyrochlore lattice and Fig. 3 shows more generally how all such processes may be described by loops, which represent the overlap of the two dimer coverings connected by the fluctuation. Here we extend the loop-graph analysis of Ref. [15] to 3D to deduce the nature of the pyrochlore ground state close to the Klein point. A perturbation  $\Delta H = \sum_{ij} \Delta J \mathbf{S}_i \cdot \mathbf{S}_j$  allows us to analyze exactly all the leading physically relevant terms in the pyrochlore Hamiltonian. Deviations from the Klein-point ratio, resulting from alterations to  $J_1$  or  $J_2$  in Eq. (3), are represented exactly by considering nearest-neighbor sites  $\langle ij \rangle$ , and deviations from  $H = H_t$ , particularly the  $J_3$  terms in Eq. (4), by using next-neighbor sites  $\langle\langle ij \rangle\rangle$ .

Loops, or dimer fluctuations, exist on all length scales, but as we show below the most important contributions

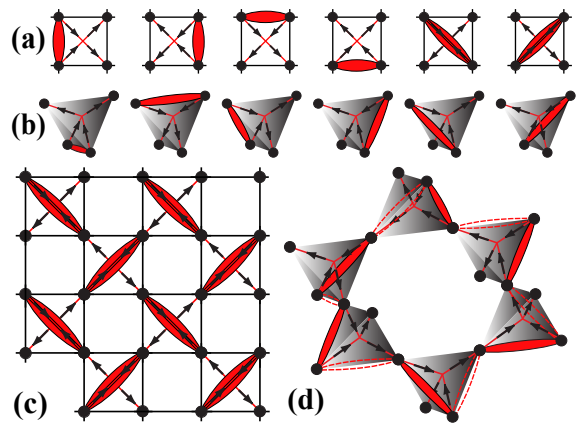


FIG. 2: (color online) One-dimer configurations on a single tetrahedron and their six-vertex representations (a) in 2D and (b) in 3D. (c) The maximally flippable state (all-diagonal dimer covering) of the checkerboard lattice, which requires only two vertex types. (d) One hexagon of the pyrochlore lattice with the dimers of the surrounding tetrahedra in a flippable configuration, as shown by the black arrows; dashed red ellipses indicate the flipped dimer state.

are made by short loops, which describe local processes. The very shortest loops in the 3D (2D) pyrochlore lattice are 12- (8)-bond paths around a single hexagon [Fig. 2(d)] (vacant square [Fig. 2(c)]). Rearranging the 6 (4) dimers corresponds to flipping the sign of the arrow in the six-vertex representation, and we refer to local dimer configurations allowing these loops as “flippable plaquettes” [Figs. 2(c) and (d)]. These “Rokhsar-Kivelson” (RK) loops are zero-energy processes [15]. Nevertheless, dimer coverings with maximal numbers of flippable plaquettes also maximize longer contributing loops and thus form the basis for the new ground states in the presence of a perturbation. In 2D, two of the vertices of the square have an “in-out” arrow configuration [Fig. 2(a)], such that regular arrays of these two can make every plaquette flippable [Fig. 2(c)]. The degeneracy of the submanifold of “maximally flippable” states is then  $\mathcal{O}(1)$ , and the ground states on both sides of the Klein point are valence-bond crystals, with a preferred static dimer order [15].

This result is a special property of the six-vertex model in a square geometry, and the situation in 3D is dramatically different. All six vertices are equivalent [Fig. 2(b)] and every tetrahedron has two edges destroying the flippability of the four associated hexagons [17], making clear that not all hexagons in the 3D pyrochlore can be flippable. Our proof of spin-liquid nature around the Klein point is the demonstration i) that the ground manifold has massive degeneracy and ii) that this degeneracy is unbroken by any of the leading quantum fluctuations.

Flippable hexagons can be counted by considering the four interlocking kagome (111) planes of the pyrochlore lattice, highlighted in different colors in Fig. 1. The max-

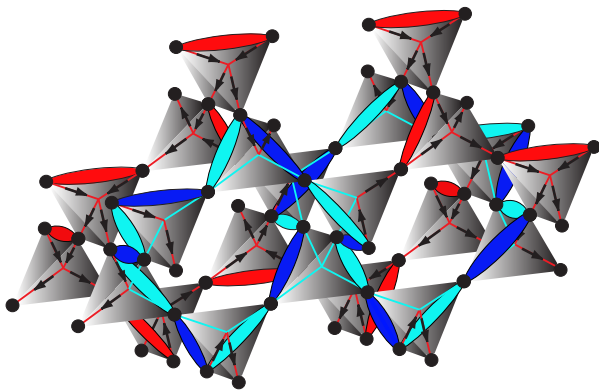


FIG. 3: (color online) Dimer fluctuation process, shown as a loop of alternating light and dark blue dimers. This is a 22-bond loop (see text).

imally flippable dimer coverings have bilayers of tetrahedra ensuring maximal flippability of the hexagons in two of the kagome planes, shown in blue and green in Fig. 1, interleaved with equivalent bilayers maximizing the other two planes (yellow and purple). The maximal number density of flippable hexagons is  $1/3$  [17]. Tetrahedra in the layer between the bilayers retain a two-fold degree of freedom in singlet orientation (Fig. 1), equivalent to the relative arrow direction between bilayers. The degeneracy of the maximally flippable manifold is then  $N_f = 9 \times 2^{L/3}$  [17], where the system volume is  $N = L^3/4$  and  $L$  is the linear dimension.

To determine the ground manifold in the presence of physical perturbations, we evaluate the matrix elements of  $\Delta H$  for each loop type; specifically, we compute  $\Delta H_{ab} = \langle \psi_a | \Delta H | \psi_b \rangle$  for states  $|\psi_a\rangle$  and  $|\psi_b\rangle$  differing by one loop of dimers (Fig. 3). The importance of the maximally flippable configurations, anticipated above, is proven by considering all loops on the pyrochlore lattice involving 2 or 3 hexagons and generated by a single RK defect. The calculations are presented in the Supplemental Material [17] and the results summarized in Table I. Beyond the RK loop, the size of the matrix elements clearly falls exponentially with loop length, demonstrating the key role of the shortest loops. The ground manifold is therefore composed of all maximally flippable states containing precisely one RK defect, which may be on any one of the  $N/3$  flippable hexagons, and hence the dimension of this manifold of basis states,

$N_p = 3N \times 2^{L/3}$ , is massive and exponential in  $L$  [17].

To construct the ground-state wave function from this manifold we require the loop density, or number of each loop type per flippable hexagon. While one type of 16-bond loop process contributes the most energy, the highest densities are found (Table I) for 22-bond loops, which correspond to flipping dimers around two hexagons sharing opposite edges of a single tetrahedron (Fig. 3). Unlike the 2D case, in 3D the lowest-order loops do interfere, and the deciding quantum fluctuations are the three shortest contributing loops in Table I [17]. By considering the most general linear combinations,  $|\psi\rangle = \sum_a c_a |\psi_a\rangle$ , of states  $|\psi_a\rangle$  based on the maximally flippable configurations with a single RK defect, we find that there are  $N_f$  distinct ground-state wave functions optimizing the loop (dimer fluctuation) contribution and that each of these is a superposition of  $\mathcal{O}(N)$  basis wave-function pairs with equal amplitudes  $|c_a|$  [17]. The sign of  $\Delta J$  causes differences not only in the phase structure of the variational wave functions (the signs of the coefficients  $\{c_a\}$ ) [15, 17] but also in their energies; we obtain  $\Delta E = -\frac{1}{256}u^2N\Delta J$  for  $\Delta J > 0$  and  $\Delta E = \frac{1}{128}v^2N\Delta J$  for  $\Delta J < 0$ , where  $u, v \simeq 1$  are normalization coefficients. Because 22-bond loops connect hexagons in neighboring bilayers, they can be used to illustrate a final, crucial property. There is no preferred direction for circumscribing a hexagon and all such loops contribute the same energy for either maximally flippable dimer covering of each bilayer. By extension to any type of interbilayer loop [17], there is no mechanism to lift the bilayer degeneracy, and hence all  $N_p$  states in the ground manifold form the same type of minimum-energy state.

To summarize, our loop calculations verify that a highly degenerate ground manifold persists under physical perturbations away from the Klein point. Further, all states in this manifold gain energy from mutual resonance. Linear combinations of these states span all dimensions and break no lattice symmetries. These are the qualitative energetic and spatial criteria for a spin liquid. However, a proof of quantum spin-liquid nature as a strict zero-temperature statement requires specific topological criteria. In the ground manifold of the non-Klein-point model, local loop processes reflect local gauge-type symmetries and their matrix elements determine the  $N_f$  variational ground states. These states are linked by  $\mathcal{O}(L^2)$  local processes, which correspond to system-scale, planar (dimension  $d = 2$ ) loops, reflecting non-local “emergent”  $\mathbb{Z}_2$  symmetries associated with each bilayer [17]. In systems of finite size, this symmetry is broken but the accompanying spectral gaps are exponentially small in  $L^2$ . The associated topological degeneracy in this and other models with  $d \geq 1$  processes [18] is analogous to 2D quantum dimer models where the ground states are also equal-amplitude superpositions of dimer coverings. These models have non-local  $d = 1$  symmetries associated with the parity of the even or odd number of dimers

TABLE I: Lowest-order loops in the pyrochlore lattice [17].

Loop Length	12	16	16	20	20	22	24	26
$\Delta H_{ab}$	0	0	$\frac{\Delta J}{128}$	0	$-\frac{\Delta J}{512}$	$-\frac{\Delta J}{1024}$	$-\frac{\Delta J}{2048}$	$-\frac{\Delta J}{4096}$
Loop Density	1	$\frac{1}{2}$	$\frac{1}{2}$	1	1	8	$\frac{1}{2}$	2

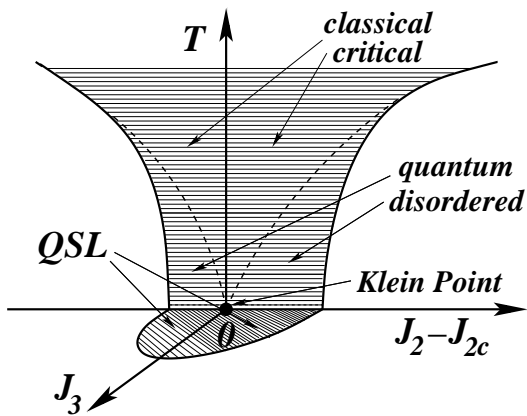


FIG. 4: (color online) Schematic phase diagram for the quantum spin liquid (QSL) phase of the  $S = 1/2$  pyrochlore.  $J_2 - J_{2c}$  and  $J_3$  represent respectively the intra- and intertetrahedron perturbations away from the Klein point. Solid lines indicate phase transitions and dashed lines crossovers.

cut by 1D loops around the entire system, and are understood as gapped quantum liquids with  $Z_2$  topological order [8]. The extension of these topological concepts to dimer states in 2D systems of real  $S = 1/2$  quantum spins has been demonstrated in recent detailed calculations [19, 20]. Our analysis provides several key additional ingredients to this discussion [17], proving rigorously from energetic and topological criteria that the pyrochlore spin model possesses zero-temperature quantum spin-liquid behavior in 3D over an extended region of the non-Klein-point parameter space, as represented in Fig. 4.

The basis states of this spin liquid are a subset of the Klein-point dimer coverings, and hence are “divergence-free” in the six-vertex arrow representation (Fig. 2). It has been argued by analogy with continuum Gaussian electrostatics that spin-ice systems can be described by a  $U(1)$  gauge field theory [17]. However, for our microscopic model, where all states in the ground manifold are known exactly, as are all loop processes connecting them (Table I), we find that the local dimer rearrangements are more complex than those of a  $U(1)$  gauge theory alone. Independent of an approximate field-theory description, the variational ground states we have constructed at finite  $\Delta J$  are an exact quantum spin liquid, meaning that states in the ground manifold are no longer individual eigenstates of the non-Klein-point Hamiltonian and are connected by quantum fluctuations to all other states in the same topological sector.

In the schematic phase diagram of Fig. 4, the solid lines indicate phase transitions, which may be of first or second order; different types of ground state become increasingly competitive as the intratetrahedron singlet-triplet energy splittings increase, but in contrast to 2D a transition requires a finite separation from the Klein point. The dashed lines indicate the energy scales for

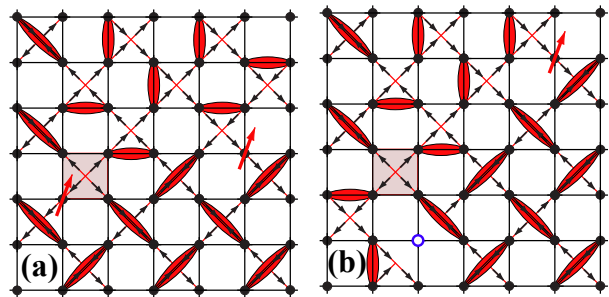


FIG. 5: (color online) Representation of (a) a dissociated spinon pair and (b) a spin-charge-separated spinon and hole.

a thermally driven crossover from quantum to classical behavior, occurring when the temperature exceeds the splitting of the Klein-point manifold and the physics of the “Coulomb phase” of spinons is restored [15]. The absolute value of this splitting is remarkable. From the matrix elements in Table I it is two orders smaller even than the perturbation  $\Delta J$ , so that, even far from the Klein point, the entire manifold would be split on an energy scale well below 1 K for any real material. The practical criterion for spin-liquid nature is that no local probe can discern any type of order. At finite temperatures, any expectation value is a Gibbs average, a sum over exponentially many states with small (or vanishing) energy splittings, and thus will vanish for temperatures above (or below) the crossover [17].

Armed with a microscopic model for a quantum spin-liquid state, we consider the nature of its excitations. High-dimensional fractionalization of both spin [15] and charge [21] degrees of freedom has been considered before in pyrochlore-based geometries. A spin excitation is the destruction of a dimer to create one defect tetrahedron (DT) and two free spins [Fig. 5(a)]. The finite energy cost for this process means these are massive spinons, with  $m_s = 15J_2/16$  [17]. From the dimensional reduction [17] in our quantum spin liquid, the spinons are constrained to move on lines [22]. In the maximally flippable ground manifold (Fig. 1), the proliferation of local loops allows spinons to move easily from one line to another [15], and therefore their motion is fully 3D. This ready availability of quantum fluctuations, exchanging spinon and dimer positions when  $H_t$  (3) is applied to individual tetrahedra [Fig. 5(a)], means that the spinons possess quantum dynamics and propagate at  $T = 0$ .

Charge degrees of freedom arise from a small concentration of dopants in the otherwise half-filled band. The energy penalty (a DT) is paid on introducing the hole, and the free spinon motion causes automatic spin-charge separation [Fig. 5(b)], leaving “holons” in the spin dimer background. Holon propagation occurs due to the kinetic term  $-t \sum_{\langle ij \rangle, \sigma} c_{i\sigma}^\dagger c_{j\sigma}$  in  $H_{\text{Hubb}}$  (1). For such a lattice model in 3D, the statistics of spinons and holons can be computed from their hopping algebra [23], but this anal-

ysis requires a detailed treatment of projection operators describing allowed states of the spin background and lies beyond the scope of the current article.

It is easy to show [17] that holons experience a weak attraction to DTs. However, a direct binding would deny the holons the kinetic energy gain of propagating, albeit with a band width highly renormalized by the spin background. Dynamical holons experiencing a mutually attractive interaction by lingering close to DTs would, by these simple considerations, have a weak tendency towards superconductivity. This superconducting state is driven not by the existence of valence-bond states [24], but by the special frustration near the Klein point.

We conclude by reviewing the possibilities for finding this spin-liquid state in a real pyrochlore material. The Klein-point value  $t/U = 1/\sqrt{30}$  is well within the parameter range of typical correlated insulators. Unfortunately, despite the wealth of pyrochlore and spinel materials available, very few structurally regular  $S = 1/2$  systems are known. A fundamental property of the model (3) is that SU(2) spin symmetry is preserved, a requirement best satisfied by magnetic ions in the  $3d$  series; to date the only candidates are the rare-earth vanadates  $M_2V_2O_7$ , which possess an additional  $t_{2g}$  orbital degeneracy and are ferromagnetic. For pyrochlores of  $4d$  ions, the SU(2) character is removed by a significant spin-orbit coupling. Among  $5d$  ions, pyrochlore iridates have received much recent attention [25] and possess an effective  $J = 1/2$  degree of freedom, but it is not possible to obtain effective SU(2)-symmetric interactions in this geometry; these materials may also be too weakly interacting (borderline metallic) to approach the magnetic limit. However, we stress again one of our key results, that energy scales for splitting of the degenerate manifold (Fig. 4) are very low, making spin-liquid behavior appear at any experimentally achievable temperatures even in systems with non-trivial perturbations from the Klein point. We suggest that pressure-dependent investigation of  $V^{4+}$  and  $Cu^{2+}$  materials may be the most promising avenue to find evidence for the spin-liquid state of the insulating spin-1/2 pyrochlore.

In summary, we have demonstrated rigorously that the half-filled one-band Hubbard model in the pyrochlore geometry hosts a 3D quantum spin liquid. This spin liquid emerges, over an extended parameter regime at zero temperature, from a highly degenerate manifold of valence-bond states. It possesses massive, deconfined spinon excitations and shows spin-charge separation on doping. It is a quantum mechanical state essentially different from those studied previously, including in the 2D pyrochlore [15]. This is one of the very few systems where unbroken degeneracies and exact deconfinement emerge in a realistic model with only short-range interactions. Finite-temperature evidence for such spin-liquid physics may be detectable in real pyrochlore materials.

We are indebted to C. Batista for his invaluable con-

tributions. We thank R. Flint, Z.-C. Gu, Z. Hiroi, G. Ortiz, C. Rüegg, S. Sachdev, A. Seidel, and T. Senthil for helpful discussions, and the Kavli Institute of Theoretical Physics for its hospitality. This work was supported by the NSF of China under Grant No. 11174365, by the National Basic Research Program of China under Grant No. 2012CB921704, and by the NSF under Grants CMMT 1106293 and PHY11-25915.

- 
- [1] P. W. Anderson, *Mater. Res. Bull.* **8**, 153 (1973).
  - [2] L. Balents, *Nature* **464**, 199 (2010).
  - [3] R. Moessner and S. L. Sondhi, *Phys. Rev. Lett* **86**, 1881 (2001); M. Hermele, T. Senthil, M. P. A. Fisher, P. A. Lee, N. Nagaosa, and X.-G. Wen, *Phys. Rev. B* **70**, 214437 (2004).
  - [4] P. Mendels and A. S. Wills, in *Introduction to Frustrated Magnetism*, eds. C. Lacroix, P. Mendels, and F. Mila (Springer, Heidelberg, 2011).
  - [5] K. Kanoda and R. Kato, *Annu. Rev. Condens. Matter Phys.* **2**, 167 (2011).
  - [6] B. Normand, *Contemp. Phys.* **50**, 4, 533 (2009).
  - [7] U. Schollwöck, *Rev. Mod. Phys.* **77**, 259 (2005).
  - [8] E. Fradkin, *Field Theories of Condensed Matter Physics*, 2nd ed. (Cambridge University Press, Cambridge, 2013).
  - [9] X.-G. Wen, *Quantum Field Theory of Many-body Systems* (Oxford University Press, Oxford, 2004).
  - [10] T. Senthil, A. Vishwanath, L. Balents, S. Sachdev, and M. P. A. Fisher, *Science* **303**, 1490 (2004).
  - [11] R. J. Baxter, *Exactly Solved Models in Statistical Mechanics* (Academic Press, London, 1982).
  - [12] D. J. Klein, *J. Phys. A Math. Gen.* **15**, 661 (1982).
  - [13] J. T. Chayes, L. Chayes, and S. A. Kivelson, *Commun. Math. Phys.* **123**, 53 (1989).
  - [14] A. Seidel, *Phys. Rev. B* **80**, 165131 (2009).
  - [15] Z. Nussinov, C. D. Batista, B. Normand, and S. A. Trugman, *Phys. Rev. B* **75**, 094411 (2007).
  - [16] L. Pauling, *The Nature of the Chemical Bond* (Cornell University Press, Ithaca, 1939).
  - [17] See Supplemental Material.
  - [18] Z. Nussinov and G. Ortiz, *Proc. Natl. Acad. Sci.* **106**, 16944 (2009).
  - [19] D. Poilblanc, N. Schuch, D. Pérez-García, and J. I. Cirac, *Phys. Rev. B* **86**, 014404 (2012).
  - [20] J. Wildeboer and A. Seidel, *Phys. Rev. Lett.* **109**, 147208 (2012).
  - [21] P. Fulde, K. Penc, and N. Shannon, *Ann. Phys. (Leipzig)* **11**, 892 (2002).
  - [22] C. D. Batista and S. A. Trugman, *Phys. Rev. Lett.* **93**, 217202 (2004).
  - [23] M. Levin and X.-G. Wen, *Phys. Rev. B* **67**, 245316 (2003).
  - [24] P. W. Anderson, *Science* **235**, 1196 (1987).
  - [25] W. Witczak-Krempa, G. Chen, Y.-B. Kim, and L. Balents, unpublished (arXiv:1305.2193).
  - [26] J. Wildeboer and A. Seidel, *Phys. Rev. B* **83**, 184430 (2011).
  - [27] C. L. Henley, *Phys. Rev. B* **71**, 014424 (2005).
  - [28] J. B. Kogut, *Rev. Mod. Phys.* **51**, 659 (1979).
  - [29] For a review see C. Castelnovo, R. Moessner, and S. L. Sondhi, *Annu. Rev. Condens. Matter Phys.* **3**, 35 (2012).
  - [30] B. Sutherland, *Phys. Rev. B* **37**, 3786 (1988); N. Read

- and B. Chakraborty, Phys. Rev. B **40**, 7133 (1989).
- [31] X.-G. Wen and Q. Niu, Phys. Rev. B **37**, 9377 (1990).
- [32] A. Kitaev, Ann. Phys. **303**, 2 (2003).
- [33] D. Rokhsar and S. Kivelson, Phys. Rev. Lett. **61**, 2376 (1988).
- [34] R. Moessner and K. S. Raman, in *Introduction to Frustrated Magnetism*, eds. C. Lacroix, P. Mendels, and F. Mila (Springer, Heidelberg, 2010).
- [35] G. Misguich and C. Lhuillier, in *Introduction to Frustrated Magnetism*, eds. C. Lacroix, P. Mendels, and F. Mila (Springer, Heidelberg, 2010).
- [36] N. Schuch, D. Poilblanc, J. I. Cirac, and D. Pérez-García, Phys. Rev. B **86**, 115108 (2012).

## SUPPLEMENTAL MATERIAL

### S1. Klein Point

The reason for the unique properties of the model for parameter values  $t/U$  ensuring  $J_2 = -J_1$  is that the Hamiltonian  $H_t$  becomes [15]

$$H_K = 6J_2 \sum_l P_{S_{l,\text{tot}}=2} = \frac{1}{4} J_2 \sum_l \vec{S}_{l,\text{tot}}^2 (\vec{S}_{l,\text{tot}}^2 - 2), \quad (5)$$

with  $\vec{S}_{l,\text{tot}}^2 = S_{l,\text{tot}}(S_{l,\text{tot}} + 1)$ . This is a sum of projectors onto the  $S = 2$  sector for each tetrahedron, meaning that all singlet and triplet states of the four spins have energy zero and the only contributions are from those tetrahedra in the quintet state. Thus any state of the whole system with one dimer singlet, formed between any two of the spins, in every tetrahedron is an exact ground state of the model [15]. This exact ground state has energy zero, as do any linear combinations of these states.

This is a Klein point [12]. The key to its exotic properties is that the ground manifold has an extensive degeneracy. The proof of extensivity lies in the exact mappings between dimer coverings, six-vertex models, and the ice rules, and is known exactly in 2D [11] and by virtue of Pauling's exponential lower bound in 3D [16]. Although the dimer coverings are not orthogonal, detailed analyses [13, 14, 26] provide strong and growing evidence that the number of linearly independent states in such a system also scales exponentially with  $N$ , and may even equal the number of dimer coverings. The most important consequence of extensive degeneracy is complete dimensional reduction [15], meaning that all states in the Klein-point manifold are connected by local (zero-dimensional) processes of dimer rearrangement. The proliferation of zero-energy local processes is responsible for the deconfinement of spinons.

The ice rules are equivalent to a zero-divergence condition, visible in the arrows of the six-vertex representation (Fig. 2), which has two immediate consequences. One is that all correlation functions are algebraic [11], with effective dipolar correlations whose nature can be made intuitive in a continuum coarse-grained representation [27].

The other is that, after expressing the divergence-free condition on the dual lattice in terms of a vector potential field, the local processes of dimer rearrangement are equivalent to  $U(1)$  gauge transformations, suggesting the nature of the associated field theory [28]. However, because every state is individually an eigenstate, the Klein point is a strange phase of matter with no quantum mechanical fluctuations [15]. The different states are connected only at finite temperatures, by thermal fluctuations, and thus it is a classical critical point. The excitations created by breaking a dimer are two massive spinons and a defect plaquette. The availability of zero-dimensional local dimer fluctuations allows the spinons and defects to propagate freely in three dimensions. The result is a two-component Coulomb gas with an entropic repulsion of deconfined spinons [15].

We comment that a subset of the concepts associated with the Klein point has been raised recently in the context of “spin-ice” pyrochlore systems and the experimental observation of “magnetic monopoles” [29]. The spin-ice pyrochlore models have semiclassical values of the magnetic moments, with Ising anisotropies and dipolar couplings, and their asymptotically deconfined monopoles are in fact a more classical version of the fully quantum spinon excitations of the present model, which predates it [15]. These systems are not candidate spin liquids.

### S2. Maximally Flippable Dimer Coverings

It is clear in 3D that all vertices of the six-vertex model are equivalent [Fig. 2(b)], in that every tetrahedron has four “in-out” edges that may contribute to a flippable hexagon and two (“in-in” and “out-out”) that destroy the flippability. Because every edge of a tetrahedron forms a part of two hexagons, it is manifestly obvious that not all hexagons in the 3D pyrochlore can be flippable. The difference between 2D and 3D lies in this fundamental geometrical property.

To count the maximal number of flippable hexagons for any possible dimer covering, we consider the four interlocking kagome (111) planes of the pyrochlore lattice, which are shown in different colors in Fig. 1. In a single kagome plane, where no hexagons share an edge but do share six-vertex lines, at most half of the hexagons may be made flippable. It is possible to form lines of flippable hexagons in two planes simultaneously, shown as blue and green in the lower part of Fig. 1, forming a zig-zag sheet of hexagons sharing one pair of edges. This maximally flippable structure occupies a bilayer of tetrahedra [Fig. 1], all of which exploit their maximal flippability (four of six edges), a situation dictating a rigid dimer configuration. Because hexagons of the other two kagome planes, shown as purple and yellow, are offset from those of the blue-green pair by one tetrahedral

unit [Fig. 1], the rigid blue-green structure excludes two bilayers of flippable purple and yellow hexagons.

This offset is the key to the maximal flippable number. By leaving a single layer of tetrahedra above and below the blue-green bilayer, the pattern may then be continued with a purple-yellow bilayer, part of which is shown at the top of Fig. 1. A single tetrahedral layer above this is then required before repeating the blue-green structure. For each kagome plane, only one hexagon in three is flippable, but this is true for all four planes. The maximal number density of flippable hexagons is therefore  $1/3$ . The bilayer offset is also the key to the degeneracy of the maximally flippable manifold. All tetrahedra in the intervening layer participate in only two flippable hexagons [Fig. 1] rather than four, and thus possess a two-fold degree of freedom. This is the orientation of the inter-bilayer singlets, or in the six-vertex representation the arrow direction around the hexagons of the upper bilayer relative to the lower. This binary choice occurs every three tetrahedral layers of the pyrochlore lattice. Because there are three primary cube axes for the layering, and there are three possible bilayers in the unit cell of Fig. 1, the final degeneracy is  $N_f = 3 \times 3 \times 2^{L/3}$ , where  $N = L^3/4$  is the system volume. The entropy of the maximally flippable manifold scales with the linear dimension  $L$  and is therefore massive.

### S3. Loops and Energetic Calculations

The quantum fluctuations of a dimer covering are local dimer rearrangement processes, which take one dimer configuration within the ground manifold into another and may be represented by closed loops [Fig. 2(d)]. The systematic procedure to account for the effects of quantum fluctuations away from the Klein point is i) to identify the leading dimer-fluctuation loops, ii) to calculate their energetic contributions in the presence of the perturbation, iii) to deduce the density of contributing loops and the variational wave functions of the states optimizing these contributions, and hence iv) to obtain the degeneracy of the new manifold of states.

*Loops and Loop Overlap.* We consider the possible loops on the pyrochlore lattice (Fig. 1). Each loop describes the overlap of two specific states, and this can be computed [15] from the length, number, and direction properties of each loop graph  $G^{ab}$  as

$$g_{ab} = \langle \psi_a | \psi_b \rangle = (-1)^{n_c + L(G^{ab})/2} 2^{N_\Gamma(G^{ab}) - L(G^{ab})/2}, \quad (6)$$

where  $L(G^{ab}) = \sum_{j=1, N_\Gamma(G^{ab})} L(\Gamma_j^{ab})$  is the total length of the graph,  $L(\Gamma_j^{ab})$  is the length of the loop  $\Gamma_j^{ab}$  within it,  $N_\Gamma(G^{ab})$  is the number of disconnected loops in the graph, and  $n_c$  is the number of arrows with clockwise circulation around the loop.

The available loops may be tabulated systematically by considering the possible connections between hexagons in

the pyrochlore geometry. Beyond the 1-hexagon RK loop (12 bonds), two hexagons may share a side (16 bonds, Fig. 6), a corner (20 bonds, Fig. 7), or opposite sides of a common tetrahedron (22 bonds, Figs. 3 and 8). As noted in the main text, the majority of loops require a single (zero-energy) RK “defect” within the maximally flippable configuration. As shown in Figs. 3 and 8, the 22-bond loop, analogous to the 14-bond loop in Ref. [15], is the first case allowing loops both with and without such an RK precursor. Loops involving 3 hexagons may also be formed around a single defect hexagon, leading to a hierarchy of possibilities sharing 2 edges (20 bonds), 1 edge and 1 corner (24 bonds), 1 edge and 1 tetrahedron (26 bonds), 2 corners (28 bonds), 1 corner and 1 tetrahedron (30 bonds), and 2 tetrahedra (32 bonds). The next families of longer loops are based on configurations involving two RK defects. The contributions from loops of all lengths may be calculated using the methods presented here.

*Loop Energy Contributions.* The calculation of matrix elements of the perturbation for each loop graph,

$$\Delta H_{ab} = \langle \psi_a | \Delta H | \psi_b \rangle, \quad (7)$$

exploits the fact that the Heisenberg term in  $\Delta H = \sum_{ij} \Delta J \mathbf{S}_i \cdot \mathbf{S}_j$  is a permutation operator exchanging sites within a loop. Thus the energy for each pair of sites  $\langle ij \rangle$  on the loop is a multiple of  $g_{ab}$ , with the prefactor taking one of only three possible values (2,  $-1$ , or  $1/2$ ) depending on the situation, and can be evaluated as a simple sum over all pairs [15]. A key property on the pyrochlore lattice is that contributions from pairs of sites on the loop with even spacings have prefactor  $+2$  and with odd spacings have prefactor  $-1$ ; because each loop passes through three sides of an average tetrahedron, with two odd spacings and one even spacing along the loop, the contribution of a “simple” loop is exactly zero. Finite energetic contributions are therefore obtained only from loops which “cross” and therefore pass through all four

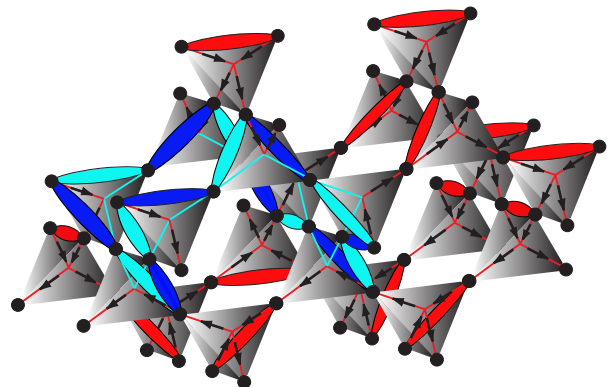


FIG. 6: (color online) Contributing two-hexagon, 16-bond dimer fluctuation process, shown as a loop of alternating light and dark blue dimers.

TABLE II: One-, two-, and three-hexagon dimer loops in the pyrochlore lattice.

Loop Length	12	16	16	20	20	22	24	24	26	26	28	30	32
$\Delta H_{ab}$	0	0	$\frac{\Delta J}{128}$	0	$-\frac{\Delta J}{512}$	$-\frac{\Delta J}{1024}$	0	$-\frac{\Delta J}{2048}$	0	$-\frac{\Delta J}{4096}$	$-\frac{\Delta J}{4096}$	$-\frac{\Delta J}{8192}$	$-\frac{\Delta J}{16384}$
Loop Density	1	$\frac{1}{2}$	$\frac{1}{2}$	1	1	4	$\frac{1}{2}$	$\frac{1}{2}$	2	2	1	8	36

sites of the same tetrahedron (Fig. 7, Fig. 3, Fig. 8), or which “touch” on two of them (Fig. 6). The matrix elements of  $\Delta H$  for all one-, two- and three-hexagon loops are shown in Table II, which is a simple extension of Table I in the main text.

*Loop Densities.* Loops will contribute to the overall energy of the wave function according to their density. Two-hexagon, 16-bond loops in the maximally flippable configuration come in two types, both with and without the pair of vertices sharing a single tetrahedron visible at the top of Fig. 6, as a result of which only half of them have a finite energy (Table II). Two-hexagon, 20-bond loops have a tightly prescribed direction. For 22-bond loops, in the maximally flippable dimer coverings (Fig. 1), eight of the 12 hexagons coupled to any given flippable hexagon are also flippable, and there are two types of loop around every pair (Figs. 3 and 8), whence the very high density. [While 32-bond loops have a still higher density, their energy is far lower.]

*Ground Manifold.* With the results of Table II it is possible to deduce the type of states appearing in the ground manifold. Clearly the maximally flippable states (Fig. 1) can only be coupled to other maximally flippable states by processes flipping an entire plane of spins, which from Eq. (6) would give an exponentially small contribution to the resonance energy. The highest energies are gained from local loop processes, and these require the presence of an RK defect, a single hexagon of flipped spins that in fact causes four of its neighboring hexagons to become unflippable. However, any such state, i.e. one with

$N/3 - 4$  flippable hexagons, is coupled to any other by all of the 16- and 20-bond loop processes and by half of the 22-bond loops (Fig. 3; the other half, shown in Fig. 8, connect states with  $N/3$  flippable hexagons to states with  $N/3 - 8$ ). Because loop energies fall by powers of 2 for every increment in loop length [Eq. (6)], states differing by two separate short loops contribute a much lower energy. Thus the ground manifold of the system is the set of maximally flippable bilayer-type states each with a single RK defect on any one of its  $N/3$  flippable hexagons, and hence  $N_p = (N/3)N_f = 3N \times 2^{L/3}$ . While loops of all lengths exist, and will contribute very small corrections to the ground-state energy, all of the qualitative features of the optimized wave function are dictated by the three shortest contributing loops, because only these connect all the states of the ground manifold (states with  $N/3 - 4$  flippable hexagons, which are also states differing only by the position of a single RK defect).

*Variational Wave Function.* The energy gain of the most general state within this ground manifold of the form  $|\psi\rangle = \sum_a c_a |\psi_a\rangle$  is given by

$$\Delta E = \frac{1}{2} \Delta J \sum_{l \neq k} c_l^* c_k g_{lk} \left[ \frac{3}{4} L(G^{lk}) - \frac{1}{2} |\mathcal{V}^{lk}| + W_{lk} \right], \quad (8)$$

where  $\mathcal{V}^{lk} = n_{ia}^{lk} + n_{ib}^{lk}$  and  $W_{lk} \equiv 2n_{ib}^{lk} - n_{ia}^{lk}$  are weights depending on the numbers of site pairs  $\langle ij \rangle$  both falling on the same loop  $\Gamma^{lk}$ , formed by overlaying the singlet dimers in states  $|\psi_l\rangle$  and  $|\psi_k\rangle$  (Figs. 3, 6–8), with odd ( $n_{ia}^{lk}$ ) or even ( $n_{ib}^{lk}$ ) separation. The overall energy gain

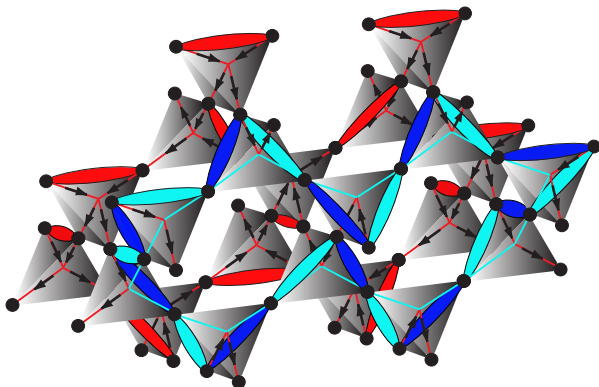


FIG. 7: (color online) Two-hexagon, 20-bond dimer fluctuation process, shown as a loop of alternating light and dark blue dimers.

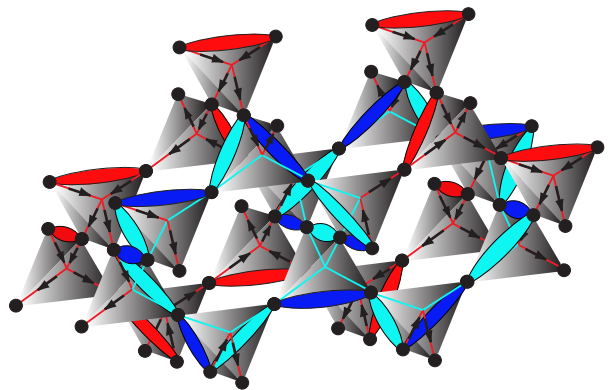


FIG. 8: (color online) Two-hexagon, 22-bond dimer fluctuation process around the same hexagons as, but distinct from, the loop in Fig. 3.



is determined from the phase structure of the coefficients  $c_a$ , which for the three shortest contributing loops can be considered as multiplicative factors for each of two RK-type flips  $|\psi_a\rangle$  of the background state, linked by the loop in question. This phase pattern must link near-neighbor hexagons throughout the system, and cannot maximize the contribution of every loop simultaneously.

The dimer coverings profiting maximally from 16-, 20-, and 22-bond processes are not the same, and not all virtual fluctuations can contribute simultaneously. The variational wave functions resulting from all of these loops consist of  $11N/2$  superposed state pairs ( $N/2$  from 16-bond loop processes,  $N$  from 20-bond loops, and  $4N$  from 22-bond loops) for each maximally flippable configuration. Thus there are  $N_f$  such variational states in the ground manifold. For  $\Delta J > 0$ , the wave functions have all  $c_a$  equal in absolute value but differing in sign according to the patterns shown in Figs. 9(a) and (b). These energetically degenerate states optimize the 16- and 20-bond loop contributions while paying a penalty from all of the intra-bilayer 22-bond loops [half of the total number of these, Fig. 9(a)], or optimize the 16- and intra-bilayer 22-bond loop contributions while paying the maximum penalty for 20-bond loops [Fig. 9(b)], to gain a total resonance energy  $\Delta E = -\frac{1}{256}u^2N\Delta J$ . When  $\Delta J < 0$ , the optimal wave functions have the phase structure depicted in Fig. 9(c), maximizing 16-, 20-, and intra-bilayer 22-bond loop contributions to gain  $\Delta E = \frac{1}{128}v^2N\Delta J$ . None of these ground-state wave functions gain energy from inter-bilayer fluctuations, whose contributions cancel due to the phase structure. The normalization coefficients  $u^2$  and  $v^2$  are  $\mathcal{O}(1)$  constants determined from the sum of all overlaps  $g_{ab}$  between the non-orthogonal dimer states [15].

*Manifold Degeneracy.* Finally, it is essential to prove that the twofold bilayer degeneracies of the maximally flippable states cannot be lifted by any interbilayer loops, i.e. that no preferred processes can lock one of the two dimer configurations to another in a neighboring bilayer. The 22-bond loop is the shortest one coupling hexagons in adjacent bilayers. For an RK defect on a hexagon in one bilayer, there are two possible loops to each adjacent bilayer, and both contribute fully for either bilayer state (direction of black arrows). No phase factors from the loop direction enter the calculation of the matrix element and no difference enters from the flippable state of either bilayer. The wave-function phases (Fig. 9) distinguish only between different pairs of hexagons, and in fact the ground states for either sign of  $\Delta J$  lead to a total cancellation of these contributions. A different argument is required to include loops connecting the bilayers through two different tetrahedra, which go beyond any of those in Table II and thus contribute exponentially lower energies. These loops exist in one spatial location only for one of the two bilayer states, and flipping the bilayer state changes the location of the loop, but

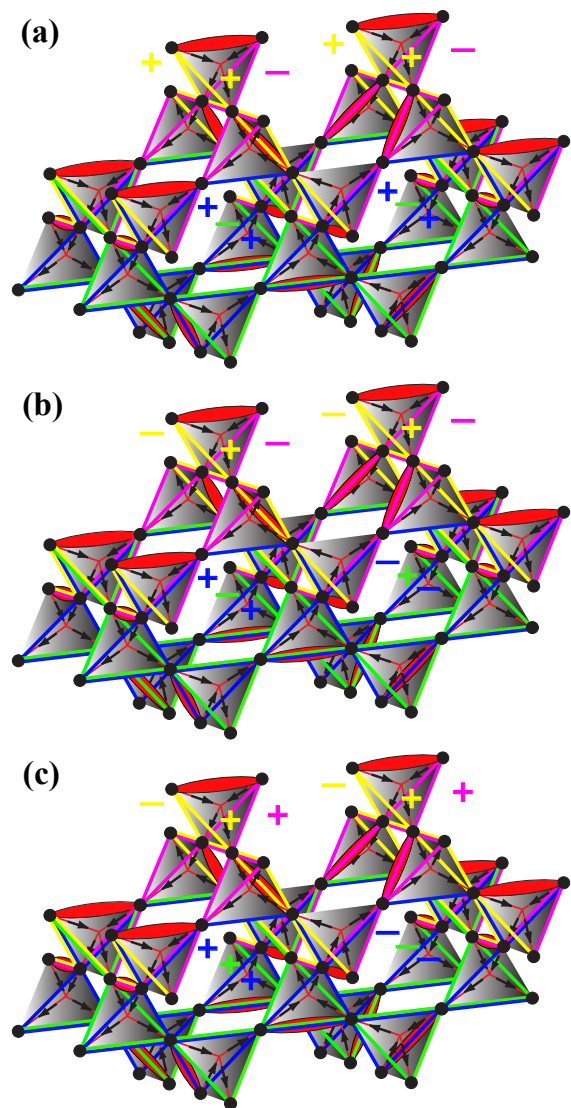


FIG. 9: (color online) Phase structure of the variational wave functions minimizing the energy for perturbations with  $\Delta J > 0$  [panels (a) and (b), which are degenerate] and with  $\Delta J < 0$  [panel (c)]. The meaning of this figure is that linear superpositions of individual wave functions (in the overall superposition) containing single RK flips linked by two-hexagon loops have relative ‘+’ or ‘-’ phases in the pattern shown.

not its length, and hence the loop energy is unchanged. Further, all such loops have multiple degenerate partners and, because their phase structure (Fig. 9) is set by the short loops, their contributions always average to the same constant (usually zero for the ground states of Fig. 9). Combinations of these two cases cover all possible inter-bilayer loop types and thus the loop energies at each order are always the same for either flippable state of each bilayer. The degeneracy of the manifold of minimum-energy states therefore remains massive, with  $N_f = 9 \times 2^{L/3}$  and an entropy scaling linearly with  $L$ . We remind the reader that this result emerges directly from a

Klein point with perturbations of both intra-tetrahedron (changes to the ratio  $J_2/J_1$ ) and inter-tetrahedron ( $J_3$ ) type, covering all the leading terms in the minimal physical model of an insulating pyrochlore magnet.

#### S4. Spin-Liquid Nature

The proof of exact spin-liquid nature at zero temperature requires both energetic and topological criteria. While several types of quantum system may have suitable energetic properties, there is now general agreement that a quantum spin liquid is a state with a specific topological order. Our spin model near the Klein point clearly satisfies all of the energetic criteria, namely the presence of a highly degenerate manifold of  $N_p$  basis states, the energy gain from resonant processes between these states, and the complete spatial symmetry of the superposition of all connected states. While the ground manifold is determined only by specific short loops, resonant processes connecting all dimer coverings in this manifold can be represented by loops of all lengths [30]. As noted above, loops of length  $L^2$  are required to mix the  $N_f$  different states of the new ground manifold, and the energetic contributions from these processes are exponentially small. While we have cut off our explicit calculations at loops of length 32 (Table II), the full ground state is a superposition (with amplitudes  $c_a$ ) of dimer states associated with arbitrarily long loops (and hence weak long-range entanglement), and the ground-state energy is a sum over all loop contributions.

These loops hold the key to the topological criteria. The existence of local loop processes reflects the presence of local (formally zero-dimensional, or  $d = 0$ ) gauge-type symmetries preserving the ice-rule conditions on the dimer arrangements. The existence of system-scale loops mixing the maximally flippable states corresponds to planar processes, which in turn are  $d = 2$  gauge-type symmetries. The symmetries associated with both types of loop are not symmetries of the Hamiltonian, but of the ground state, and in this sense they are “emergent” at the lowest energies. The Klein-point manifold is split on an energy scale of order  $-\Delta J/100$  (Table II), with  $N_f$  degenerate states at the bottom of the spectrum. These states are connected only by planar processes, loops with lengths of order  $L^2$  in a finite system, which [following Eqs. (6) and (8)] have energies of order  $-\Delta J/2^{L^2}$ , and this type of exponentially small spectral gap is associated with topological order [18, 31]; similar exponentially small differences arise also in measurements for other quasi-local operators. In the topologically ordered system, local loops are processes within the same topological sector while system-scale loops are topological operations that change this sector. In a finite system there are  $N_f = 9 \times 2^{L/3}$  such sectors, which can be prescribed by the states of an Ising chain with  $L/3$  sites ( $L/3$   $Z_2$  variables, i.e. an

emergent  $Z_2 \otimes Z_2 \otimes \dots \otimes Z_2$  symmetry). The parities of the bilayers in each sector and the symmetries of the processes connecting them determine the topological order and spin-liquid behavior, as in other known spin liquids including the Toric code model [32] and quantum dimer models [33].

Indeed the situation is closely analogous to the discussion of dimer-liquid states in quantum dimer models, where the ground-state wave function is a superposition of dimer coverings with equal amplitude but differing phases, often referred to as the short-range resonating valence-bond (RVB) state. Quantum dimer models in 2D (3D) possess  $d = 1$  ( $d = 2$ ) gauge-type symmetries associated with the even or odd number of dimers cut by a line (plane) circumscribing the system, which specifies a parity, or  $Z_2$  variable. The topological sector cannot be changed by local processes, but can be altered by nontrivial, system-length loop processes, and the 2 (3) independent cycles determine a topological degeneracy of  $2^2$  ( $2^3$ ); for comparison, in the present model there are  $L/3$  cycles. Quantum dimer models exhibit quantum liquid behavior with a finite gap,  $Z_2$  topological order, and fractionalized excitations [34]. An extensive body of literature exists linking these topological concepts to the properties of RVB states in physical systems based on real  $S = 1/2$  quantum spins, and we cite only some recent contributions [8, 19, 20, 35, 36]. The pyrochlore spin model away from the Klein point provides an important additional dimension to these studies by presenting a demonstrably exact situation where a real  $S = 1/2$  system possesses all of the energetic and topological properties of a zero-temperature quantum spin liquid.

From a practical standpoint, the issue of most relevance is the behavior of the system at finite temperatures,  $0 < T \ll \Delta J$ . An experimental definition of spin-liquid nature is that no local measurement can distinguish between ground states, in any topological sector, and thus no local probes may discern any type of order. Spin-liquid character can be quantified using the density matrix and the finite-temperature expectation values of local observables. Any expectation value is a Gibbs average over exponentially many states with infinitesimal energy splittings, whose density matrix has the form of an equal-amplitude sum of all admissible states in a given topological sector. This is precisely the canonical form of known spin-liquid wave functions (we cite again the examples of the Toric code and quantum dimer models), also at zero temperature. At finite temperatures, the expectation value of any quantity not invariant under all local symmetries must vanish by Elitzur’s theorem. In this case, in contrast to the  $T = 0$  case, it is the local gauge-type symmetries corresponding to the presence of local loop processes that determine the topological quantum order [18]. Further, when  $\Delta J \ll T \ll E_g$ , where  $E_g$  denotes the spectral gap between states in the Klein-point manifold and all other states, then the local symmetries

determined by the ice rules emerge. This is the situation above the dashed lines in Fig. 4. Here again, Elitzur's theorem dictates that only observables invariant under this increased number of local symmetries may attain a non-trivial expectation value.

### S5. Spinon and Holon Energies

To explore the energetics of spinons and holons, we neglect the weak next-neighbor interaction ( $J_3$ ) and begin by considering a defect tetrahedron (DT). Because an energy penalty is incurred only by the five quintet states (out of the 16 possible states) of a tetrahedron with four uncorrelated spins, the energy cost of a DT is  $E_{\text{dt}} = 5/16 \cdot 6J_2 = 15J_2/8$ . Spinons are uncorrelated  $S = 1/2$  objects [Fig. 5(a)], which incur no penalty if they occupy a tetrahedron containing a dimer and do not change the energy of a DT if they remain on it. Hence the mass of one spinon is  $m_s = 15J_2/16$  and their motion once created is entirely free. As stated in the main text, the spinons are deconfined in the spin-liquid state.

The introduction of a single hole creates a DT with a free spin, which may propagate freely with no energy change. A hole on a DT forms a tetrahedron with total spin  $S_{l,\text{tot}} = 1/2$  or  $3/2$  (each with probability  $1/2$ ), plus a neighboring tetrahedron with one dimer and  $S_{l,\text{tot}} = 1/2$ , whence from Eq. (5)  $E_{\text{bh}} = [3E(S_{l,\text{tot}} = 1/2) + E(S_{l,\text{tot}} = 3/2)]/2 = 15J_2/32$ . A hole in a singlet background separated from its DT creates two  $S_{l,\text{tot}} = 1/2$  tetrahedra and therefore has an energy  $E_{\text{fh}} = -15J_2/32$ ; because  $E_{\text{dt}} + E_{\text{fh}} = 45J_2/32$ , there is a holon-DT binding energy of  $15J_2/16$ . Similarly, two “free” holons separated from their DT have a total energy  $E_{2\text{fh}} = 15J_2/16$ , one free and one bound holon have total energy  $E_{\text{fh}} + E_{\text{bh}} = 0$ , and two holons on the same DT have total energy  $E_{2\text{bh}} = 0$ . Thus the “potential” part of the effective dimer-spinon-holon Hamiltonian contains an attractive interholon interaction. In the event that this interaction leads to superconductivity of dynamical holons, if these have bosonic statistics they would condense individually, while fermionic holons would pair and then condense.